



MODELING OF EVAPORATION FROM NANOPOROUS MEMBRANES USING MOLECULAR DYNAMICS SIMULATION

Yiğit AKKUŞ

ASELSAN A.Ş. Haberleşme ve Bilgi Teknolojileri Sektör Bşk., 06370 Yenimahalle, Ankara
yakkus@aselsan.com.tr

(Geliş Tarihi: 30.12.2018, Kabul Tarihi: 20.03.2019)

Abstract: Evaporation from nanoporous structures is widely studied theoretically and experimentally due to its huge potential in thermal management of high heat flux electronic devices. Yet a fundamental understanding of liquid-vapor interfacial transport is lacking due to the absence of a molecular/atomic level modeling framework. In the current study, a computational setup is constructed to model the steady-state, continuous evaporation from a single nanopore, which is analogous to a nanoporous membrane due to the utilization of proper periodic boundary conditions. Under increasing heat loads, shape and position of the evaporating meniscus are observed, and different evaporation regimes (pinning and receding) are identified. An uncommon, self-regulation of the meniscus during receding is discovered and the underlying physical mechanism is elucidated. Heat removal ability of the nanopore is examined in response to different operating conditions. To the best of the author knowledge, the current study is the first attempt to model the evaporation from a nanoporous membrane incorporating non-continuum effects associated with the both liquid and vapor flows. The methodology presented opens up an avenue for the molecular/atomic level modeling of evaporation from nanoporous membranes.

Keywords: Evaporation, nanoporous membrane, molecular dynamics simulation, self-regulation of an evaporating meniscus.

NANO-GÖZENEKLİ ZARLARDAN GERÇEKLEŞEN BUHARLAŞMANIN MOLEKÜLER DİNAMİK SİMÜLASYONLARI KULLANILARAK MODELLENMESİ

Özet: Nano-gözenekli yapılardan gerçekleşen buharlaşma, yüksek ısı akısına sahip elektronik cihazların ısı yönetimindeki büyük potansiyeli nedeniyle teorik ve deneysel olarak geniş çapta incelenmektedir. Fakat moleküler/atomik seviye bir modelleme yönteminin eksikliği sebebiyle, sıvı-gaz arayüzünde gerçekleşen taşımının temellerinin anlaşılabilmesi mümkün olamamaktadır. Bu çalışmada, uygun periyodik sınır koşullarının kullanımı sayesinde nano-gözenekli bir zarı betimleyebilen bir tekil nano-gözenekten gerçekleşen buharlaşmayı modelleyen bir hesaplama düzeneği oluşturulmuştur. Artan ısı yükleri altında, buharlaşan menisküsün şekli ve konumu gözlenmiş ve farklı buharlaşma rejimleri (çivilenmiş ve çekilen) tanımlanmıştır. Genel olarak bilinenin aksine, menisküsün çekilme sırasında kendi şeklini değiştirdiği keşfedilmiş ve bu duruma sebep olan fiziksel mekanizma açıklanmıştır. Nano-gözenekğin ısı uzaklaştırabilme kabiliyeti, farklı çalışma koşulları altında incelenmiştir. Yazarın bilgisine göre, bu çalışma, hem sıvı hem de buhar akışı ile ilgili olan sürekli-olmayan-ortam etkilerini göz önüne alarak nano-gözenekli bir zardan buharlaşmayı modelleyen ilk girişimdir. Sunulan yöntem, nano-gözenekli zarlardan gerçekleşen buharlaşmanın moleküler/atomik seviyede modellenemesinin önünü açmaktadır.

Anahtar Kelimeler: Buharlaşma, nano-gözenekli zar, moleküler dinamik simülasyonu, buharlaşan menisküsün kendi şeklini değiştirmesi.

INTRODUCTION

Evaporation from porous structures is the key mechanism behind numerous natural phenomena such as water transpiration in plants (Wheeler and Stroock, 2008). It is also applied in various industrial applications including water desalination (Lee *et al.*, 2014; Nguyen and Beskok, 2018) and microelectronics cooling (Plawsky *et al.*, 2014). Today, energy dissipation of integrated circuits is one of the greatest challenges which limit the performance of electronic devices (Pop, 2010) and the realization of next-generation electronic and photonic

devices is possible only with the significant enhancements in cooling performances (Garimella *et al.*, 2008). The capability of removing a large amount of energy, which is stored in the form of latent heat, makes evaporation process an effective cooling method. Various thermal management devices, such as heat pipes and vapor chambers, use evaporation of liquid, which is supplied by porous wicks, as the heat removal mechanism from electronics.

During the evaporation process from a liquid-vapor interface, heat is transferred to the free surface *via* the

conduction path through the liquid in the absence of any convective energy transport, which inevitably creates a temperature difference between the liquid-vapor interface and substrate. This temperature difference should be kept as low as possible to lower the temperature of the substrate if the evaporation is utilized to cool down the substrate or any component in contact with the substrate. Thickness of the liquid block, therefore, is desired to be small to reduce the conductive thermal resistance. Thermal scientists have long been investigating the characteristics of thin film evaporation (Wayner *et al.*, 1976; Moosman and Homsy, 1980; Stephan and Busse, 1992; Akkuş *et al.*, 2017). Thin film evaporation studies concentrate on identification and characterization of heat transfer near the contact line (the intersection of liquid, solid and gas phases), where the liquid forms a micro/nano scale film, and, accordingly, evaporation rates are elevated. Liquid is delivered to this region, often called as micro-region in heat transfer community, by mainly capillary pumping, *i.e.* the pressure difference resulting from the deformation of interface. While capillary pumping scales inversely with capillary size, viscous resistance, which increase with the square of the capillary size, counteracts the flow (Dullien, 1992). This balance usually limits the size of the capillary structures utilized in porous membranes for two-phase cooling (Palko, 2015). Although substantial effort has been devoted to increase capillarity and, hence, evaporative heat fluxes, utilizing extremely hydrophilic nano- and micro-engineered surfaces (Ding *et al.*, 2010; Weibel *et al.*, 2011; Cai and Bhunia, 2012; Coso *et al.*, 2012), ultimate liquid transport has remained restricted due to the coupling between capillary pressure and viscous resistance.

Decoupling of viscous losses and high capillary pressure can be achieved by reducing the length of the flow path. Recent advances in MEMS/NEMS based fabrication techniques enable the production of nanoporous membranes with extremely small thicknesses (Xiao *et al.*, 2013; Wilke *et al.*, 2017; Lu *et al.*, 2017), which significantly decreases the viscous resistance along the flow path. Reduced flow path together with the extreme capillary pressure generated by nanoscale cavities result in the removal of high heat fluxes with moderate temperature differences, *i.e.* superheats. For instance, nanoporous membranes (50 μm -thick) produced in 2013 by Xiao *et al.*, were able to dissipate heat fluxes up to $\approx 96 \text{ W/cm}^2$ at the expense of superheats lower than 50°C . In a recent study (Lu *et al.*, 2017), on the other hand, 200 nm-thick nanoporous membrane was produced, and this membrane was able to dissipate heat fluxes up to $\approx 500 \text{ W/cm}^2$ at the expense of superheats lower than 70°C . In both studies, effective pore radius was at the order of 100 nm. It should be noted that the great potential of nanoporous structures for the efficient pumping of liquid has been already revealed in the literature. For example, the pressure drop within nanoscale capillaries was demonstrated to be higher than 100 kPa, which, in fact, renders the absolute liquid pressure to negative values (Scholander *et al.*, 1965; Wheeler and Stroock, 2008). In this state, the liquid, which is under tension, is

thermodynamically metastable with respect to its own vapor (Caupin and Herbert, 2006) and is prevented from the cavitation due to the length scale of the capillary, which is smaller than critical cavitation radius (Fisher, 1948).

Modeling of evaporation and associated liquid flow in nanoporous membranes is not a straightforward task due to the deviations from continuum predictions. Density (Ghorbanian *et al.*, 2016) and apparent viscosity (Vo *et al.*, 2015) depart from their bulk fluid properties at the nanoscale. The effect of interfacial thermal resistance (Kapitza resistance) becomes significant (Shi *et al.*, 2012) for the high heat flux applications commonly present at the molecular level. Liquid-solid contact angle displays significant variations (Barisik and Beskok, 2013) and liquids exhibit severe density oscillations (molecular layering) due to the wall-force-field effect (Heslot *et al.*, 1989; Cheng *et al.*, 2001) at the nanoscale. Vapor flow in nano-conduits necessitates kinetic theory based modeling in either the transition or free molecular flow regimes (Barisik and Beskok, 2011). While molecular/atomistic level modeling can incorporate all of the aforementioned nanoscale effects, there exist a few continuum-based studies to model the evaporation from a single nanopore (Narayanan *et al.*, 2011; Lu *et al.*, 2015). Among these studies, the only study that considered nanoscale effects was the one conducted by Lu *et al.* in 2015, where nonequilibrium effects arising from the deviations from classical kinetic theory for the vapor flow were incorporated in modeling. However, liquid transport was still analyzed using continuum approach.

The current study, basically, aims to investigate the evaporation from a nanoporous structure using molecular dynamics. The cell structure (a single nano-conduit) used in this study mimics a complete nanoporous membrane due to the utilization of periodic boundary conditions. To the best of the author knowledge, a steady-state, continuous and molecular/atomic level modeling of evaporation from a nanoporous structure is absent in the literature. The current study fills this gap and presents a useful computational setup that can be used in further studies focusing on evaporation from nanoporous structures.

METHOD

Modeling of steady-state evaporation requires continuous removal of atoms/molecules. Previous studies targeting to investigate the evaporation process (Maroo and Chung, 2010; Yu and Wang, 2012) were able to observe the interfacial transport for a limited time span and the total number of fluid atoms was decreasing during the simulations. However, fluid atoms can be entirely consumed or fall below a certain quantity, which may not be sufficient to perform a reliable statistical averaging, before the establishment of a steady evaporation. In order to obtain a steady-state operation, which conserves the total number atoms/molecules, a

recently proposed phase change driven pumping methodology (Akkus and Beskok, 2019) is utilized.

The nano-conduit is constructed by placing two parallel solid Platinum (Pt) walls as shown in Figure 1a. The capillary is filled with fluid (Argon) atoms. The system is simulated using molecular dynamics (MD). Simulation domain is restricted by the outermost Pt layers of each wall in y -direction. Length of the domain in x -direction is the twice of the wall length. The detailed geometry and dimensions of the system are provided in Figure 1a. The number of Argon (Ar) atoms is determined after a meticulous iterative process. First, an approximate number of atoms is placed to create a saturated liquid-vapor mixture at the prescribed simulation temperature. A part of Ar atoms condenses to liquid phase within the capillary due to the interaction of fluid atoms with solid wall atoms. Other fluid atoms occupy rest of the simulation domain as the vapor phase. Number of Ar atoms is, first, iterated such that liquid phase is attached to the channel corners at the inlet and outlet after the equilibration period (Figure 1b-c). Then phase change induced pumping is initiated by equally heating and cooling the solid atoms in heat injection and extraction regions, respectively. While evaporation leads to the loss of liquid mass at the evaporator side, the liquid accumulates at the condenser. Liquid-vapor interface at the condenser part should be nearly flat to mimic a liquid reservoir beneath the membrane. Therefore, the amount of Ar atoms is subjected to a final iteration to obtain the desired interface at the condenser. Other details of the process and MD simulations are provided in the following section.

Molecular Dynamics Simulation Details

The computational setup has two parallel walls composed of $(3240 \times 2 = 6480)$ Pt atoms. Each wall has 4 solid layers packed in FCC (face-centered cubic) crystal structure and $(1,0,0)$ crystal planes meet the liquid. The outermost layer of the walls is kept at their lattice position to preserve the boundaries of the simulation domain. 4200 Ar atoms are utilized for the fluid. Lennard-Jones (L-J) 6-12 potential is used to model the interactions between Ar-Ar and Ar-Pt atoms:

$$\phi(r_{ij}) = 4\epsilon \left[\left(\frac{\sigma}{r_{ij}} \right)^{12} - \left(\frac{\sigma}{r_{ij}} \right)^6 \right] \quad (1)$$

The values for interaction diameter between Ar atoms ($\sigma_{\text{Ar}} = 0.34$ nm) and depth of the potential well for Ar ($\epsilon_{\text{Ar}} = 0.01042$ eV) are well-defined in the literature and experimental confirmation was also made (Barker and Pompe, 1967). Pt-Pt atomic interactions are modeled using embedded atom model (Foiles *et al.*, 1986). For Pt-Ar interactions, different parameters exist in the literature (Maroo and Chung, 2008; Yu and Wang, 2012; Peng *et al.*, 2014). In the current study, interaction diameter ($\sigma_{\text{Ar-Pt}} = 0.3085$ nm) and depth of the potential well ($\epsilon_{\text{Ar-Pt}} = 0.00558$ eV) are selected following the study of Maroo and Chung, 2008, which chose the values based on a previous study (Maruyama and Kimura, 1999) utilizing Lorentz rule (Lorentz, 1881) for the combination. Cut-off distance for the truncation of L-J potential is $3\sigma_{\text{Ar}}$. This

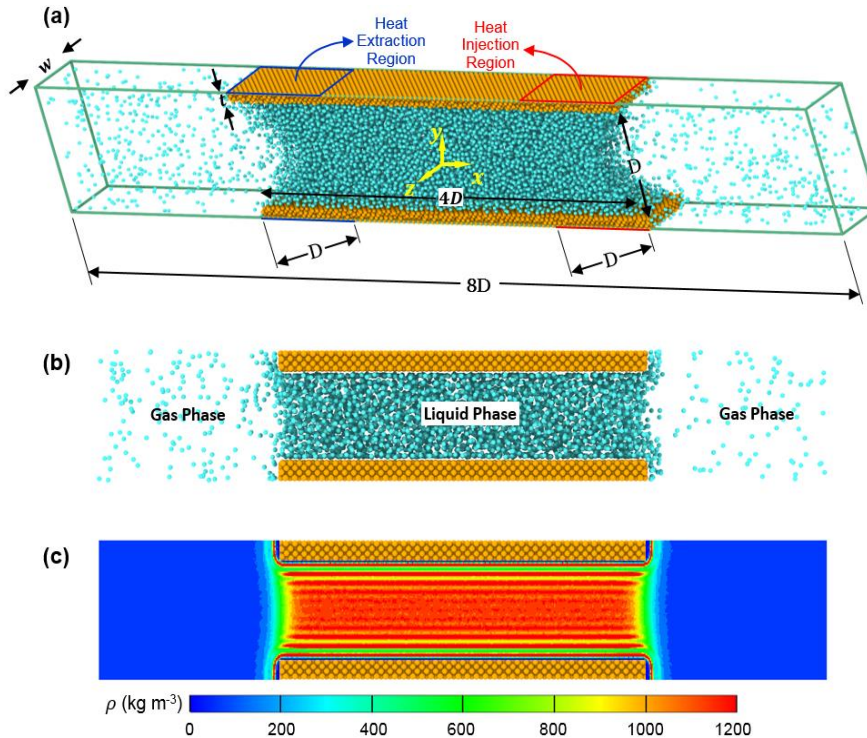


Figure 1. (a) Schematic of the computational setup. Yellow and turquoise spheres demonstrates Platinum and Argon atoms, respectively. The channel height (D) and wall depth (w) are 3.92 nm. Thickness of the wall (t) is 0.94 nm. (b) A snapshot of the system during isothermal operation. (c) Time-averaged density distribution of Argon during isothermal operation. Molecular layering resulting from wall-force-field effect is prominent near the walls.

value is determined based on preliminary simulations carried out for liquid Argon confined between Pt walls by varying cut-off distance for LJ interactions. Liquid bulk density is measured during simulations, and, beyond the cutoff distance of $3\sigma_{Ar}$, no significant deviation from thermodynamical value is detected.

Simulations are initiated from the Maxwell-Boltzmann velocity distribution for all atoms at 110 K. Simulation times are selected such that sufficient numbers of measurements for fluid and flow properties are made to secure accurate statistical averaging. Except the atoms in the outermost Pt layers, all atoms are subjected to Nosé-Hoover thermostat for 15 ns to stabilize the system temperature at 110 K. Then thermostat is removed for fluid atoms and NVE ensemble is applied for 15 ns to equilibrate the system. Following thermostating and equilibration periods, stable liquid-vapor interfaces are attained at the ends of the nano-conduit at 110 K (Figure 1c). Then the second part of the simulation is started by applying equal energy injection/extraction to the solid atoms located at the heat injection and extraction regions for 40 ns (Figure 2a). The wall atoms, which are not located at the heat injection/extraction regions, are not allowed to vibrate in order to eliminate the heat conduction through the walls. During this period, fluid atoms are subjected to NVE ensemble. Different heat loads are applied to observe the response of liquid-vapor interfaces. Heating rates below 6 nW yield neither a flat interface at the condenser nor substantial meniscus deformation at the evaporator. Heating rates above 11 nW, on the other hand, lead to a jump in evaporation resistance, which is accepted as the indication of burnout. Therefore, the heating rates between these limits ($\dot{q}=6, 7, 8, 9, 10$ and 11 nW) are applied throughout the study. At the end of heating/cooling period, statistically stable phase changing liquid/vapor interfaces are formed at both

ends of the nano-capillary (Figure 2b). During the simulations, time step is set as 5 fs and each collected data is averaged for 2 ns. Periodic boundary conditions are applied in all directions. All simulations are performed using Large-scale Atomic/Molecular Massively Parallel Simulator (LAMMPS) (Plimpton, 1995). Computations are carried out using high performance parallel computing. Optimum number of cores used in the simulations is determined *a priori*, based on preliminary simulations. Total simulation time for thermostating, equilibration and heating/cooling periods is nearly 18 hours.

Fluid Selection

Accurate statistical averaging requires sufficient number of atoms in vapor phase, which can be realized by selecting a liquid with high vapor pressure. Although water is a commonly used liquid in engineering applications including the evaporation from nanoporous structures, it is not suitable for MD simulations due to its relatively low volatility. For example, saturated liquid-vapor mixture of water at room temperature has the ratio of $\sim 1/50,000$ vapor to total water molecules. Therefore, for a simulation carried out in a nanoscale domain, there would never be enough water molecules in the gas phase. Multiplication of the total number of water molecules, on the other hand, is not possible due to limitation of computational power. In the present study, Argon is selected as the working fluid since it has high volatility and well-defined atomic interactions (Barker and Pompe, 1968). Moreover, the current computational setup is effective as long as the liquid wets the walls of the nano-conduit, and argon displays wetting characteristics on a Pt wall.

RESULTS AND DISCUSSION

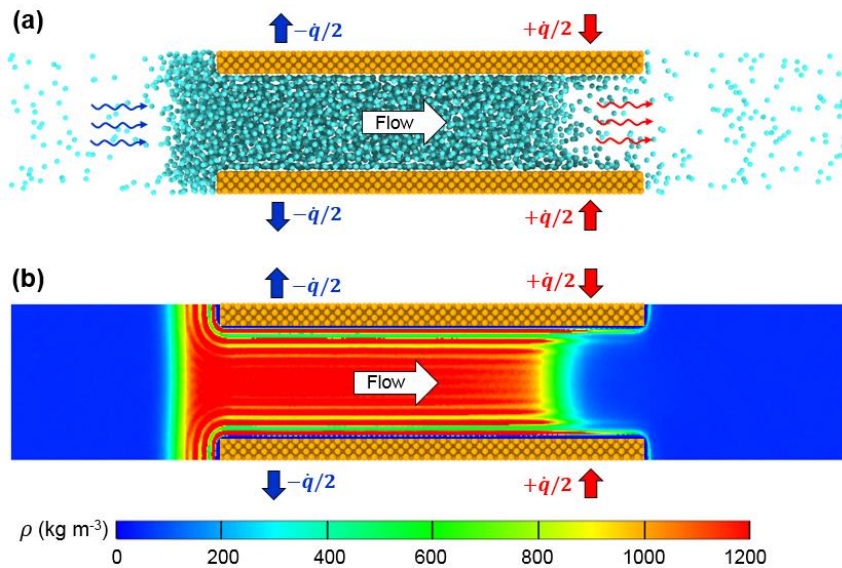


Figure 2. (a) A snapshot of the system during heating/cooling period. (b) Time-averaged density distribution of Argon during heating/cooling period.

The current study utilizes periodic boundary conditions (PBCs) at all boundaries of the simulation domain. Using PBCs has advantages such as eliminating the surface effects and keeping the same number of molecules within the simulation domain. On the other hand, application of PBCs in all directions is geometrically equivalent to replication of the simulation domain throughout the space to form an infinite lattice (see Figure 3a). Each lateral layer in this infinite structure is, actually, equivalent to a membrane composed of an infinite array of nanopores as shown in Figure 3b.

Continuum assumption in the modeling of vapor flow requires the Knudsen number to be sufficiently small (generally, less than 0.01), *i.e.* representative physical length scale should be sufficiently larger than the molecular free path of gas atoms. Mean free path for a Boltzmann gas can be calculated based on kinetic theory as follows:

$$\lambda = \frac{k_B T}{\sqrt{2} \pi d^2 p} \quad (2)$$

where k_B , d , T , and p are Boltzmann constant, effective diameter for the gas molecule, temperature and pressure of the gas, respectively. Effective diameter of the gas molecule can be taken as Van der Waals diameter of the molecule, which is practically the same with the interaction diameter (σ_{Ar}) between Ar atoms used in L-J potential. During the application of maximum heating rate ($\dot{q}=11$ nW), at which liquid is substantially receded

into the capillary, mean free path of a gas molecule inside the capillary is approximately 2.6 nm, which is comparable with the distance between the two walls (see Figure 3c). It should be noted that mean free path is calculated based on gas properties averaged in the bulk gas phase above the evaporating interface, and its value can vary based on the selection of the gas region, where averaging is performed. However, regardless of the variation of its value, mean free path of a gas molecule in the current study is always at the same order of the size of the capillary. Therefore, continuum level modeling of gas flow is not appropriate for the present nanopore or for the ones with smaller diameter. Moreover, modeling of evaporation from a single nanopore may not be sufficient to mimic the evaporation from a nanoporous membrane since the evaporation from neighboring pores, *i.e.* the vapor molecules emitting from adjacent pores, can significantly influence the vapor flow over the nanopore of interest.

The shape and position of the liquid-vapor interface changes in response to different heating conditions. Self-regulation of the meniscus has been widely studied in the literature both theoretically and experimentally (Nilson *et al.*, 2006; Nie *et al.*, 2013; Guo *et al.*, 2015; Lu *et al.*, 2015). Under the increasing heat input, meniscus is shown to deform by diminishing its radius of curvature while it is still attached to the edge of the capillary. During this deformation, the edge angle between the wall of the capillary and liquid interface decreases until the edge angle reaches the contact angle of the liquid on the solid substrate, *i.e.* wall. Further heating results with the

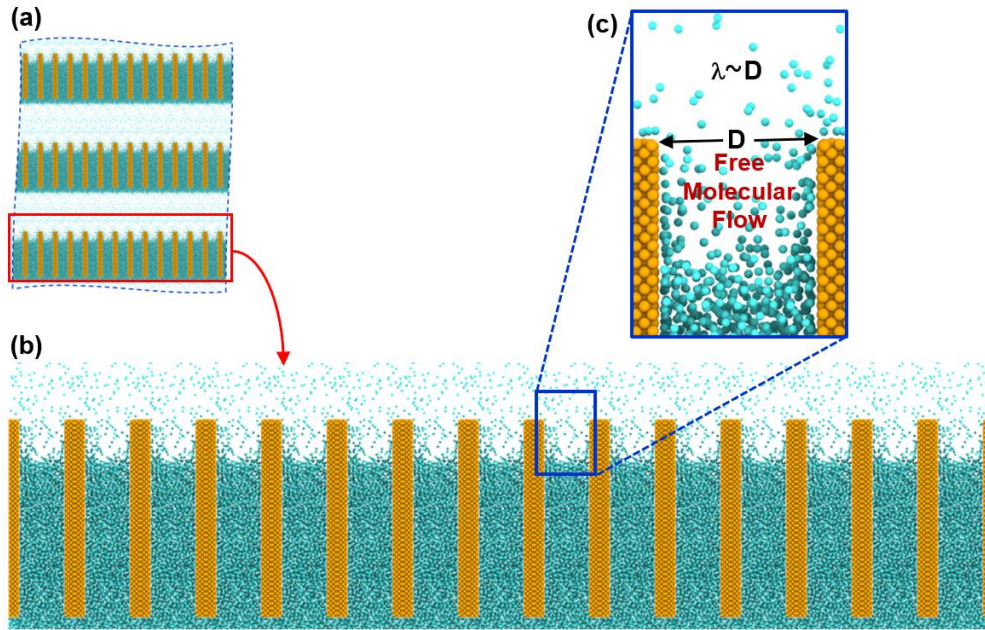


Figure 3. (a) Periodic images of the simulation domain. While periodic images create an infinite lattice, a sample region is captured in the figure. (b) A sample nanoporous membrane from the infinite lattice. The lower part of membrane can be considered to be fed by a liquid reservoir since it has a nearly flat liquid-vapor interface. (c) Gas flow within the nano-capillary. Free mean path of a gas molecule is smaller than the effective diameter of the capillary resulting a free molecular flow inside the nano-conduit.

detachment of the meniscus from the edge of the capillary and meniscus recedes into the capillary while preserving its shape. Evaporation takes place regardless of the configuration of the meniscus. However, the effectiveness of the evaporation may be influenced based on the position of the meniscus. In order to evaluate the effectiveness in response to this regime change, a non-dimensional performance parameter is utilized (Wilke *et al.*, 2017; Akkus *et al.*, 2019). The parameter is defined based on the ratio of actual evaporation rate to the maximum theoretical mass flow rate. Actual evaporation rate is equal to the liquid mass flow rate through the capillary (\dot{m}_l) due to the steady-state operation. Maximum theoretical mass flow rate, on the other hand, can be calculated assuming that all the heat input given to the system is utilized to evaporate the liquid, *i.e.* conduction through axial direction is zero. Then the parameter for the effectiveness of evaporation (Π) can be defined as follows:

$$\Pi = \frac{\dot{m}_l}{\dot{q} h_{fg}} \quad (3)$$

where h_{fg} is the latent heat of evaporation at the temperature of the gas phase above the evaporating meniscus and \dot{q} is the heating rate. During the calculation of evaporation effectiveness, uncertainty is associated with the liquid mass flow, which is calculated based on the measurements of the axial velocity and density at the mid-plane of the capillary. Evaporation effectiveness values corresponding to different heating rates are given in Figure 4a. While the heating rates between 6 and 9 nW yield similar values, effectiveness starts to decrease for the heating rates higher than 9 nW. In order to assess the relation between the meniscus shape and effectiveness, time-averaged density distributions at different heating rates are superimposed on Figure 4a. For the highest heat inputs, detachment of meniscus from the wall edges is observed, which can be considered as a reasonable explanation of the lower evaporation effectiveness at these heating rates. Meniscus is able to increase the

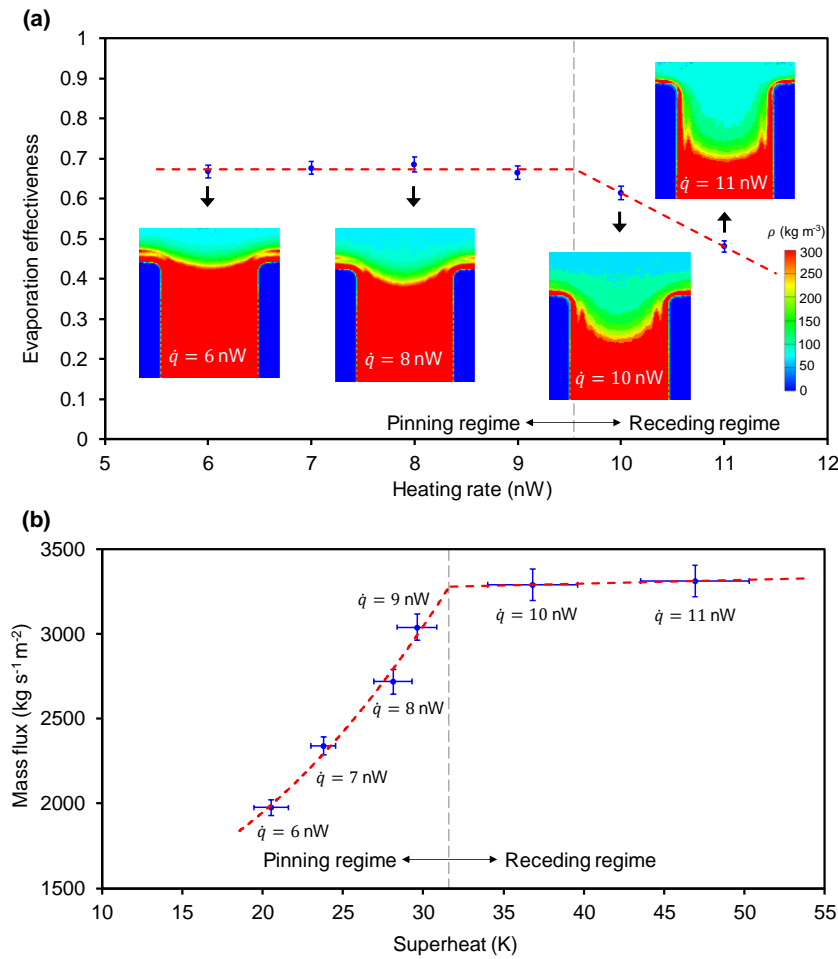


Figure 4. (a) Variation of the effectiveness of evaporation, Π , with respect to the heating rates, \dot{q} . Red dashed lines are linear fittings to the data. Time-averaged density distributions at different heat loads are superimposed. Cut-off density for the interface is selected as 300 kg m^{-3} , which is slightly higher than the density of the first minimum density peak in the liquid phase, to obtain a continuous liquid-vapor interface. (b) Variation of the evaporation mass flux and corresponding superheats at different heating rates. Red dashed lines are second order and linear fittings to the data at pinning and receding regimes, respectively.

capillary pumping rate by adjusting its curvature during the heating as long as it is pinned to the corners. However, after the disconnection of meniscus from the corners, meniscus is expected to recede into the capillary without changing its curvature (Nilson *et al.*, 2006). Therefore, liquid flow rate does not change significantly regardless of the increase in heating rates resulting a lower effectiveness. To identify the pinning and receding regimes, linear fittings are applied to the data groups with higher and lower effectiveness as show by red dashed lines in Figure 4a. While the evaporation effectiveness is almost constant for lower heating rates, a decreasing pattern is apparent for higher rates. Intersection of two trend-lines demonstrates the switch from the pinning regime to receding regime. Since the evaporation from nanoporous membranes has a great potential for the cooling applications, a relevant performance indicator is their ability to sustain high evaporation fluxes with small superheats, *i.e.* the temperature differentials between the heated solid substrate and vapor phase. In Figure 4b, evaporation mass fluxes and corresponding superheats at different heating rates are provided. While evaporation rate and superheat proportionally increases in response to the increase in heating rate during the pinning regime, evaporation rate slightly increase in the expense of an extensive rise in the superheat suggesting a highly inefficient cooling performance. A relevant plot was reported by Lu *et al.* in 2015, where they modeled the evaporation from nanopores with the minimum hydraulic diameter of 20 nm due to the continuum restrictions in liquid flow. In order to compare the present results with study of Lu *et al.*, second and first order fittings are applied to the data groups of pinning and receding regimes, respectively. A similar variation of evaporation mass flux with respect to superheat and a similar regime shift are observed as shown in Figure 4b.

During the receding of meniscus, capillary pumping ability is expected to remain the same due to the unchanging profile of the liquid-vapor interface. The liquid mass flow, on the other hand, can still slightly increase (Lu *et al.*, 2015) due to the diminishing viscous losses resulting from the shortening of liquid flow path. In the current study, a slight increase in liquid mass flow rate (evaporation rate) is observed during receding of the meniscus, which might be, normally, attributed to diminishing viscous losses. However, surprisingly, profile of the liquid-vapor interface is not similar for the cases with heating rates of 10 and 11 nW. Strikingly, meniscus becomes flattened at the heating rate of 11 nW compared to the profile at 10 nW, suggesting a decrease in capillary pumping, and, consequently, a reduction in liquid mass flow rate. The increase of liquid mass flow rate, despite the reduction of capillary pumping, suggests the presence of another mechanism responsible for the passive pumping of the liquid. A recent MD study conducted by YD and Maroo in 2016 demonstrated that

passive flow of liquid adjacent to a solid substrate with a substantial temperature gradient occurs due to the variation of solid-liquid surface tension. In the present study, adsorbed liquid films form on the walls of the capillary after the receding of meniscus at 11 nW heating rate as shown in Figure 4a. A passive flow resulting from the variation of solid-liquid surface tension contributes to the capillary pumping, which leads to the flattening of the meniscus profile.

Although the maximum evaporating mass flux is obtained for the highest heating rate ($\dot{q}=11$ nW), the maximum heat flux occurs at the heating rate of 10 nW due to the changes in latent heat of evaporation in response to varying system temperature. The maximum heat flux achieved is approximately 42.0 kW/cm², which is a tremendously high value for an evaporation process. Estimation of the theoretical limit of evaporation based on kinetic theory was suggested by Gambill and Lienhard in 1989, and, accordingly, kinetic limit is calculated as 44.2 kW/cm² in the current study, which is slightly higher than the heat flux obtained in the simulation, exhibiting the huge potential of evaporation from nanoporous membranes for the cooling applications. The radius of curvature during the maximum heat removal was at the same order of the effective radius of the capillary (~ 1.96 nm), which corresponds to a pressure reduction of ~ 3.6 MPa beneath the liquid-vapor interface. Since the vapor pressure is nearly ~ 1.4 MPa at this heating rate, the absolute liquid pressure is around -2.2 MPa near the interface even in the absence of disjoining pressure, which, indeed, would lower the liquid pressure further. Negative absolute liquid pressures at the similar order of magnitudes were demonstrated by previous MD studies for Ar (Maroo and Chung, 2010). Cavitation within the liquid is prevented due to the length scale of the capillary, which is smaller than critical cavitation radius, $R_c = -2\gamma/p_l$, (Fisher, 1948). While the length scale of the capillary is 3.92 nm in the current study, critical cavitation radius is approximately ~ 6.5 nm.

CONCLUSION

A computational setup was presented to model the steady state, continuous evaporation from nanoporous membranes. Evaporation from a single nanopore, which successfully mimics a complete membrane, was simulated using molecular dynamics. Morphological changes on the evaporating meniscus were observed during the application of increasing heat loads. Different evaporation regimes (pinning and receding) were identified. During the pinning regime, evaporation rates increased due to the adjustment of the radius of curvature of the meniscus. After the meniscus was fully extended, it receded into the nanopore and evaporation rates were slightly enhanced, suggesting a more effective heat removal in the pinning regime. Contrary to the conventional understanding, the self-regulation of the meniscus during the receding regime was discovered and

the physical mechanism behind this observation was elucidated. Maximum heat flux achieved during the simulations was calculated ($\sim 42.0 \text{ kW/cm}^2$) and found to be very near the theoretical limit ($\sim 44.2 \text{ kW/cm}^2$).

ACKNOWLEDGEMENT

The author would like to thank Prof. Ali Beskok for his guidance during the study. Computations were carried out using high performance computing facilities of Center for Scientific Computation at Southern Methodist University.

REFERENCES

- Akkuş Y., Tarman I. H., Çetin B. and Dursunkaya Z., 2017, Two Dimensional Computational Modeling of Thin Film Evaporation, *Int. J. Therm. Sci.*, 121, 237-248.
- Akkus Y. and Beskok A., 2019, Molecular Diffusion Replaces Capillary Pumping in Phase-change-driven Nanopumps, *Microfluid. Nanofluid.*, 23, 14.
- Akkus Y., Nguyen C. T., Celebi A. T. and Beskok A., 2019, A First Look at the Performance of Nano-grooved Heat Pipes, *Int. J. Heat Mass Trans.*, 132, 280-287.
- Barisik M. and Beskok A., 2011, Molecular Dynamics Simulations of Shear-driven Gas Flows in Nano-channels, *Microfluid. Nanofluid.*, 11, 611-622.
- Barisik M. and Beskok A., 2013, Wetting Characterisation of Silicon (1, 0, 0) Surface, *Mol. Simul.*, 39, 700-709.
- Barker J. A. and Pompe A., 1968, Atomic Interactions in Argon, *Aust. J. Chem.*, 21, 1683-1694.
- Cai Q. and Bhunia A., 2012, High Heat Flux Phase Change on Porous Carbon Nanotube Structures, *Int. J. Heat Mass Tran.*, 55, 5544-5551.
- Caupin F. and Herbert E., 2006, Cavitation in Water: A Review, *C. R. Phys.*, 7, 1000-1017.
- Cheng L., Fenter P., Nagy K. L., Schlegel M. L. and Sturchio N. C., 2001, Molecular-scale Density Oscillations in Water Adjacent to a Mica Surface, *Phys. Rev. Lett.*, 87, p.156103.
- Ćoso D., Srinivasan V., Lu M. C., Chang J. Y. and Majumdar A., 2012, Enhanced Heat Transfer in Biporous Wicks in the Thin Liquid Film Evaporation and Boiling Regimes, *J. Heat Transf.*, 134, p.101501.
- Ding C., Soni G., Bozorgi P., Piorek B. D., Meinhart C. D. and MacDonald N. C., 2010, A Flat Heat Pipe Architecture Based on Nanostructured Titania, *J. Microelectromech. S.*, 19, 878-884.
- Dullien F. A. L., 1992, *Porous Media: Fluid Transport and Pore Structure*, 2nd ed., Academic Press.
- Fisher J. C., 1948, The Fracture of Liquids, *J. Appl. Phys.*, 19, 1062-1067.
- Foiles S. M., Baskes M. I. and Daw M. S., 1986, Embedded-atom-method Functions for the Fcc Metals Cu, Ag, Au, Ni, Pd, Pt, and Their Alloys, *Phys. Rev. B*, 33, p.7983.
- Gambill W. R. and Lienhard J. H., 1989, An Upper Bound for the Critical Boiling Heat Flux, *J. Heat Transf.*, 111, 815-818.
- Garimella S. V., Fleischer A. S., Murthy J. Y., Keshavarzi A., Prasher R., Patel C., Bhavnani S. H., Venkatasubramanian R., Mahajan R., Joshi Y. and Sammakia B., 2008, Thermal Challenges in Next-generation Electronic Systems, *IEEE Transactions on Components and Packaging Technologies*, 31, 801-815.
- Ghorbanian J., Celebi A. T. and Beskok A., 2016, A Phenomenological Continuum Model for Force-driven Nano-channel Liquid Flows, *J. Chem. Phys.*, 145, p.184109.
- Guo C., Yu D., Wang T., Jiang Y. and Tang D., 2015, Theoretical and Experimental Analysis of the Evaporating Flow in Rectangular Microgrooves, *Int. J. Heat Mass Trans.*, 84, 1113-1118.
- Heslot F., Fraysse N. and Cazabat A. M., 1989, Molecular Layering in the Spreading of Wetting Liquid Drops, *Nature*, 338, 640-642.
- Lee J., Laoui T. and Karnik R., 2014, Nanofluidic Transport Governed by the Liquid/vapour Interface, *Nature Nanotechnol.*, 9, 317-323.
- Lu Z., Narayanan S. and Wang E. N., 2015, Modeling of Evaporation from Nanopores with Nonequilibrium and Nonlocal Effects, *Langmuir*, 31, 9817-9824.
- Lu Z., Wilke K. L., Preston D. J., Kinefuchi I., Chang-Davidson E. and Wang E. N., 2017, An Ultrathin Nanoporous Membrane Evaporator, *Nano Lett.*, 17, 6217-6220.
- Maroo S. C. and Chung J. N., 2010, Heat Transfer Characteristics and Pressure Variation in a Nanoscale Evaporating Meniscus, *Int. J. Heat Mass Trans.*, 53, 3335-3345.
- Maruyama S. and Kimura T., 1999, A Study on Thermal Resistance over a Solid-liquid Interface by the Molecular Dynamics Method, *Therm. Sci. Eng.*, 7, 63-68.
- Moosman S. and Homsy G. M., 1980, Evaporating Menisci of Wetting Fluids, *J. Colloid Int. Sci.*, 73, 212-223.

Narayanan S., Fedorov A. G. and Joshi Y. K., 2011, Interfacial Transport of Evaporating Water Confined in Nanopores, *Langmuir*, 27, 10666-10676.

Nguyen C. T. and Beskok A., 2018, Saltwater Transport through Pristine and Positively Charged Graphene membranes, *J. Chem. Phys.*, 149, p.024704.

Nie X., Hu X. and Tang D., 2013, Modeling Study on Axial Wetting Length of Meniscus in Vertical Rectangular Microgrooves, *Appl. Therm. Eng.*, 52, 615-622.

Nilson R. H., Tchikanda S. W., Griffiths S. K. and Martinez M. J., 2006, Steady Evaporating Flow in Rectangular Microchannels, *Int. J. Heat Mass Trans.*, 49, 1603-1618.

Palko J. W., Zhang C., Wilbur J. D., Dusseault T. J., Asheghi M., Goodson K. E. and Santiago J. G., 2015, Approaching the Limits of Two-phase Boiling Heat Transfer: High Heat Flux and Low Superheat, *Appl. Phys. Lett.*, 107, p.253903.

Peng B., He W., Hao X., Chen Y. and Liu Y., 2014, Interfacial Thermal Conductance and Thermal Accommodation Coefficient of Evaporating Thin Liquid Films: A Molecular Dynamics Study, *Comp. Mater. Sci.*, 87, 260-266.

Plawsky J. L., Fedorov A. G., Garimella S. V., Ma H. B., Maroo S. C., Chen L. and Nam Y., 2014, Nano-and Microstructures for Thin-film Evaporation—A Review, *Nanosc. Microsc. Thermophys. Eng.*, 18, 251-269.

Plimpton S., 1995, Fast Parallel Algorithms for Short-range Molecular Dynamics, *J. Comput. Phys.*, 117, 1-19.

Pop E., 2010, Energy Dissipation and Transport in Nanoscale Devices, *Nano Res.*, 3, 147-169.

Scholander P. F., Bradstreet E. D., Hemmingsen E. A. and Hammel H. T., 1965, Sap Pressure in Vascular Plants: Negative Hydrostatic Pressure can be Measured in Plants, *Science*, 148, 339-346.

Shi Z., Barisik M. and Beskok A., 2012, Molecular Dynamics Modeling of Thermal Resistance at Argon-graphite and Argon-silver Interfaces, *Int. J. Therm. Sci.*, 59, 29-37.

Stephan P. C. and Busse C. A., 1992, Analysis of the Heat Transfer Coefficient of Grooved Heat Pipe Evaporator Walls, *Int. J. Heat Mass Trans.*, 35, 383-391.

YD S. and Maroo S. C., 2016, Origin of Surface-driven Passive Liquid Flows, *Langmuir*, 32, 8593-8597.

Vo T. Q., Barisik M. and Kim B., 2015, Near-surface Viscosity Effects on Capillary Rise of Water in Nanotubes, *Phys. Rev. E*, 92, p.053009.

Wayner P.C., Kao Y. K. and LaCroix L. V., 1976, The Interline Heat-transfer Coefficient of an Evaporating Wetting Film, *Int. J. Heat Mass Trans.*, 19, 487-492.

Weibel J., Garimella S. V., Murthy J. Y. and Altman D. H., 2011, Design of Integrated Nanostructured Wicks for High-Performance Vapor Chambers, *IEEE Transactions on Components Packaging and Manufacturing Technology*.

Wheeler T. D. and Stroock A. D., 2008, The Transpiration of Water at Negative Pressures in a Synthetic Tree, *Nature*, 455, 208-212.

Wilke K. L., Barabadi B., Lu Z., Zhang T. and Wang E. N., 2017, Parametric Study of Thin Film Evaporation from Nanoporous Membranes, *Appl. Phys. Lett.*, 111, p.171603.

Xiao R., Maroo S. C. and Wang E. N., 2013, Negative Pressures in Nanoporous Membranes for Thin Film Evaporation. *Appl. Phys. Lett.*, 102, p.123103.

Yu J. and Wang H., 2012, A Molecular Dynamics Investigation on Evaporation of Thin Liquid Films, *Int. J. Heat Mass Trans.*, 55, 1218-1225.



Yigit AKKUŞ is a senior engineer in ASELSAN A.Ş. He received his B.Sc. and minor degrees from the Mechanical Engineering and Materials and Metallurgical Engineering Departments of Middle East Technical University, Ankara, Turkey, in 2009, respectively. He obtained his Ph.D. degree from the Mechanical Engineering Department of Middle East Technical University in 2015. He was a post-doctoral fellow in Mechanical Engineering Department of Southern Methodist University, Dallas, U.S.A., in 2017-2018. Dr. Akkuş is responsible for the thermal management and packaging of high heat flux electronics in ASELSAN. His research focuses on macro-, micro- and nano-scale heat transfer, two-phase passive heat spreaders, thin film evaporation and condensation, droplet evaporation and molecular dynamics simulations. He currently teaches “AAR-652 Passive Heat Exchange Devices and Phase Change” course in ASELSAN Academy.